Annealing studies of boron implanted emitters for n-silicon solar cells

Peng Liang[1], Peide Han, Fan Yujie and Yupeng Xing

State Key Laboratory on Integrated Optoelectronics, Institute of Semiconductors, Chinese Academy of Sciences, No. 35A Qinghua East Road, Haidian District, Beijing 100083, People's Republic of China

E-mail: liangpeng@semi.ac.cn

Abstract

Effects of annealing on the properties of B-implanted Si for n-type solar cells were investigated by comparing rapid thermal annealing (RTA) and furnace annealing (FA) conditions. Profiles of boron and residual damage were theoretically simulated by technology computer aided design based on boron diffusion kinetics mechanism of transient enhanced diffusion. Compared with the rapid thermally annealed samples, the furnace annealed one showed the lowest remnant damage spectra obtained by channeling Rutherford backscattering spectrometry. Furthermore, the electrical properties of boron implanted samples were characterized by Hall and QSSPC technique, revealing a trend that increasing annealing thermal budget would result in higher active carrier density and lower emitter saturation current density. Finally, passivated emitter solar cells were fabricated to verify the influence of annealing conditions on the performances at device level. The champion cell with efficiency of 18.85% received FA for 20 min, whereas those with lower thermal budgets exhibited significantly lower performance. From diode parameters obtained by fitting dark I–V curves and short wavelength responses of internal quantum efficiency spectrum, it was found that B-implanted samples required an annealing temperature of at least 1000 °C together with a sufficiently long time. Rather low thermal budget such as RTA for dozens of seconds was far enough to realize full activation of boron and removal of implantation damage.

Keywords: boron implanted emitter, implantation damage, n-silicon, rapid thermal annealing, TCAD simulation

(Some figures may appear in colour only in the online journal)

1. Introduction

Ion implantation, as a clean and simple way of doping in the conventional microelectronics industry, has long been deemed inappropriate for fabricating large-scale power generating devices such as solar cells because of its low throughput and high energy expenditure. However, the surge in demand for high-efficiency low-cost solar cells in recent years has fueled rapid development of ion implantation technique in the photovoltaic community [1], because of its multiple advantages over the conventional tube furnace diffusion process: improved junction quality through precise dopant control, excellent surface passivation and blue response due to

the removal of 'dead layer' that is common to furnace diffusion and great simplicity for selective doping with independent optimization. All these pronounced merits make it compelling that more optimal cell design with potentially higher cell efficiency is in sight by way of implantation. Until very recently ion-implanter specially tailored for PV applications has been commercially available [2] and used to fabricate solar cells with very low saturation current densities and high efficiency above 20% [3, 4].

As a great amount of accelerated ions are bombarded into the silicon, silicon atoms are inevitably collided away from their equilibrium lattice sites, giving rise to point defects in the form of vacancies and self-interstitials. This lattice structural damage will annihilate very rapidly upon annealing at elevated temperatures, leaving, in principle, one Si

---

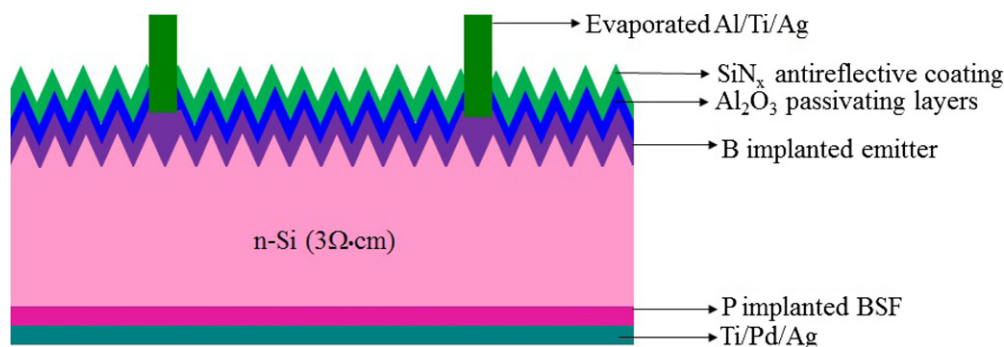[1] Author to whom any correspondence should be addressed.

Figure 1. Schematic drawing of PESCs with phosphorus implanted BSF.

self-interstitial for each substitutional implanted ion. Accordingly, annealing exerts a strong influence on the degree of damage removal and dopant activation, and furthermore, the quality of implanted region and performance of responding devices. To determine the most appropriate annealing condition for solar cell fabrication, various annealing techniques have been investigated in the past years including pulsed excimer laser annealing [5], flash lamp annealing [6], flame annealing [7], electron beam annealing [8], two-step furnace annealing (FA) [9], rapid thermal annealing (RTA) [10], etc. However, those novel techniques are limited to laboratory investigation instead of mass production due to their inherently multiple problems such as immature technology keypoints, complexity of manipulation and low degree of reproducibility. We therefore devote our main effects to conducting an attentive study on conventional RTA and FA, both of which are feasible for the present industrial production line.

In this paper, boron implanted p-type emitter in passivated emitter solar cells (PESCs) is specially investigated with an aim to exploiting the effect of RTA and FA on the electrical property of emitters and the performance of devices. Emphasis is put on physical explanation of annealing thermal budget dependent cell efficiency. In addition, powerful process simulation tools of TCAD (technology computer aided design) software, is applied to theoretically identify the emitter doping profiles and remnant damage profiles at various annealing conditions.

2. Experimental details

The 1 cm^2 all-implanted p$^+$-n-n$^+$ solar cells were uniformly positioned on 2 inch n-type CZ wafers with resistivity of 3 $\Omega \cdot$ cm and thickness of 380 μm. After inverted pyramidally texturing of the polished sunward surface by lithographic process, the wafers received boron implantation with dose of 1e15/cm^2 and acceleration energy of 30 keV through isolation windows in the front and phosphorus implantation with dose of 3e15/cm^2 in the whole back surface. All the as-implanted wafers subsequently underwent four different annealing processes in flowing inert atmosphere: RTA (at 900 °C, 30 s; 1000 °C, 10 s; 1000 °C, 30 s) and FA (at 1000 °C, 20 min). It is noteworthy that a total of 12 wafers were simultaneously processed in order to allocate three wafers in each annealing condition for experimental

uncertainty concerns. Then all the annealed samples were passivated by Al$_2$O$_3$ films deposited by thermal atom-layer-deposition system with thickness of about 15 nm and further capped by plasma-enhanced chemical vapor deposited (PECVD) silicon nitride (SiN$_x$) with thickness about 60 nm as antireflective coating. Photolithography defined contact stripes of 8 μm width were opened in the front dielectric films. Backside metallization consisted of thermally evaporated Ti–Pd–Ag metal stacks. Al–Ti–Ag multilayer metals were then evaporated successively by e-beam equipment over the whole front surface and electrode pattern was successfully realized by wet chemical lift-off process in acetone. The gridlines were finally thickened by plating up to 10 μm to reduce resistive loss from the electrode. A cross section of the device is schematically shown in figure 1.

3. Theoretical simulation and emitter characterization

3.1. Simulation of dopant profiles after RTA and FA processing

To gain a deepgoing understanding of the physical mechanism that dominates boron diffusion and activation kinetics, accurately simulating dopant diffusion profile and damage evolution based on experimental data is necessary in that one can relate the experimentally determined electrical parameters of emitters to the microscopic evolution mechanism of damage created by implantation. In this regard, Florakis *et al* have conducted a detailed analysis of the impact of different annealing conditions on the emitter saturation current density [11]. It is well known that transient enhanced diffusion (TED) of implanted samples usually happens in RTA [12], which makes it rather difficult in accurate modeling of boron doping profiles. This phenomenon stems from the huge supersaturation of point defects introduced by ion implantation in the originally perfect crystalline and leads to an anomalous broadening of the dopant profile in a short period during the high-temperature annealing process. Based on the SSUPREM4 models developed by Stanford university [13], the simulated doping profiles in the inset of figure 2 show perfect matching with measured data obtained by secondary ion mass spectroscopy (SIMS). Some models mainly adopted in simulation include: full coupled diffusion model allowing for the interaction of dopants and nonequilibrium point defects,
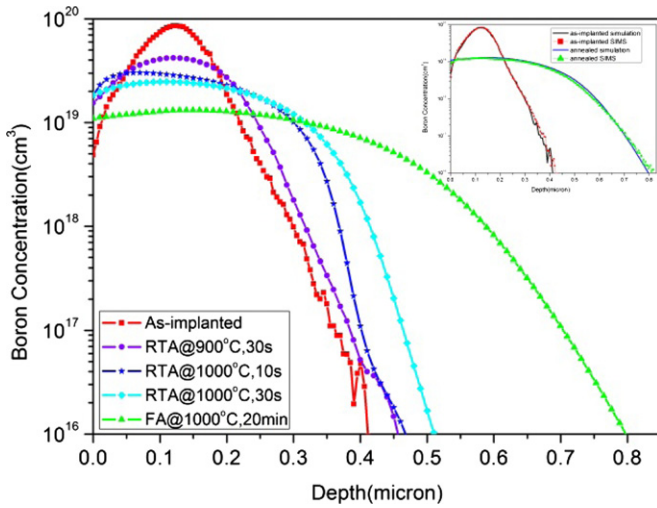
Figure 2. Simulated profiles of active boron after annealing at different conditions. The as-implanted and FA boron profiles illustrated in the inset gives excellent match between SIMS measurement and TCAD simulation.

Figure 3. Plots of remnant cluster concentration of the as-implanted and four annealed samples. The parameters used to generate the figure are calibrated by fitting simulated boron profile to SIMS data.

{3 1 1} cluster damage model accounting for the evolution of interstitial clusters, high concentration model describing the higher-order pairing of defect-dopant/defect.

From the simulated boron profiles plotted in figure 2, we observe obvious enhanced diffusion occurring at a temperature of 1000 °C in the first few seconds. Prolonging annealing time makes the dopants migrate quickly into the deeper region, resulting in a lowered surface concentration and an increased profile depth. This is because B diffuses largely by the interstitialcy mechanism [14], the time varying excessive point defect populations can enhance the dopant diffusivity at elevated temperature. In addition, emitters with RTA processing are characterized by a slight 'recession electric field' in 0.1 μm range of near silicon surface, which is incurred by difference of ionized boron concentration in surface and internal peak. This disadvantageous field prohibits the collection of photogenerated electrons by junction and results in increased surface recombination and degradation of emitter quality. Only after a sufficiently long time of annealing can this effect be eliminated.

The damage creation mechanism can be simply described as follows: a beam of accelerated boron ions entering the crystalline silicon will slow down or be scattered due to the nuclear collision and electronic interaction. Along each ion's projectile, recoiling atoms can induce collision cascades of moving targeted atoms, resulting in local compositional change or lattice distortion. Bombarded silicon atoms, originally positioned at their balance, displace from the normal lattice sites and leave point defects (a pair of interstitial and vacancy). As the implantation dose increases, this significant amount of excessive point defects superposes and gathers, creating interstitial clusters, which can evolve from small ones to rod-like clusters with bigger size lying on {3 1 1} planes of the silicon matrix and finally to end-of-range (EOR) dislocation loops primarily present at the interface of the original amorphized layer and the underlying substrate, where space charge region (SCR) lies. These extended volume
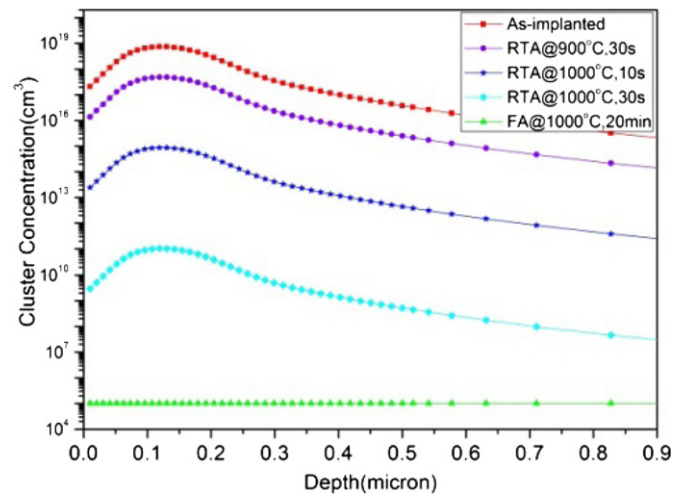
defects can be thought of as small pockets of interstitials that can trap or release Si interstitials during annealing. Since the implantation of boron is non-amorphizing for doses below 2e16/cm^2 [15], a large amount of clusters and point defects are present in the implanted region, forming effective recombination centers for free carriers. The evolution of interstitial {3 1 1} clusters with annealing temperature and time abide by the following equation:

$$\frac{\partial C_{cluster}}{\partial t} = f(x) \times \left(\frac{1}{\tau}\right) \exp\left(-\frac{t}{\tau}\right), \quad (1)$$

where $f(x)$ is the as-implanted profile of {3 1 1} clusters, τ is an Arrhenius type temperature dependent time constant. As can be seen from figure 3, increasing the thermal budget in RTA will greatly reduce the amount of clusters. After FA at 1000 °C for 20 min, the residual clusters are sufficiently annealed out. Furthermore, other forms of defects like BICs (boron-interstitials-clusters) [16] or EOR dislocation loops [17] exhibit more complicated evolving mechanisms than {3 1 1} clusters [18]. Commonly they show stable characteristic even at temperature up to 1000 °C, giving rise to a drastic increase of SRH recombination rate in the emitter.

3.2. Measurement of Rutherford backscattering

Random and channeling RBS measurements were performed to determine the disordering of the annealed samples using 2 MeV He$^+$ ions beam incident on the (1 0 0) surface of the samples. The backscattered yield was collected by a circular detector with an energy resolution close to 30 keV. Figure 4 gives the energy spectra of random and channeling RBS of the perfect crystal and four samples annealed at different thermal budgets. The 'random' signal height represents an amorphous layer where all Si atoms are displaced, while the 'channeling' spectra stands for the background from a perfect crystalline substrate. The spectra for the four annealed samples reflect the disordering of the lattice sites when He$^+$ ions are incident in channeling direction. Each spectra of annealed sample consists of a He$^+$ ions scattered peak from surface implanted region and
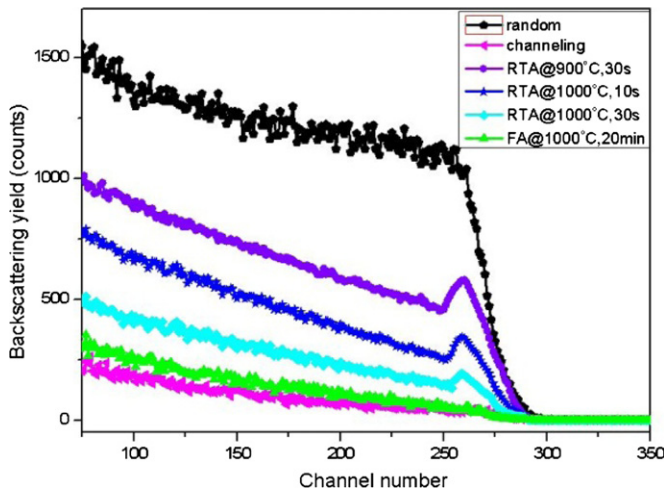
Figure 4. Rutherford backscattering channeling spectra from boron implanted samples prepared under different annealing conditions.
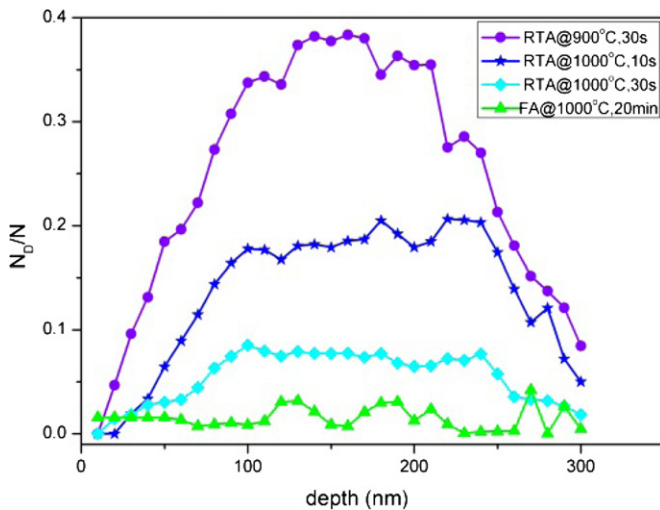

Figure 5. Damage profiles for boron implanted samples with 1e15/cm^2 dose as function of annealing condition.

a dechannelling tail. As shown in figure 4, channeling spectra recorded from sample annealed in furnace for 20 min is nearly indistinguishable from the perfectly crystalline. In contrast, the other three samples (by RTA) show obvious surface peaks, suggesting that a disordered layer is present in boron implanted emitter. Based on classical theory of Rutherford backscattering [19], we can transform the surface peak in channeling spectra (scattering yields versus channeling number) into disorder profile in the implanted region with x-axis the implantation depth and y-axis the normalized amount of damage, as depicted in figure 5. The position of damage peak of each spectra satisfies well with the projected range (R_P) of SIMS measurement in figure 2. By comparison, we can observe a trend that the damage signal around R_P decreases with increasing thermal budget. Obviously, annealing at 1000 °C for 20 min reduces this signal near to zero, indicating a sufficient annihilation of implantation damage. There are several possible sources of remnant damage that contribute to the disorder spectra: displaced silicon atoms, complex clusters of boron-silicon interstitials, clusters of silicon interstitials,

Table 1. Hall measurement of boron implanted samples annealed at different conditions.

Annealing condition	Sheet carrier density (/cm^2)	Mobility (cm^2/V · s)	Sheet resistance (Ω/□)
As-implanted	1.092e14	73.7	507
900 °C, 30 s	1.767e14	62.7	226
1000 °C, 10 s	4.069e14	55.8	187
1000 °C, 30 s	7.135e14	49.5	154
1000 °C, 20 min	9.873e14	35.1	128

dislocation loops and distortion of an otherwise crystalline lattice. The various forms of damage mainly locate in the range of 0.3 μm near the top of the silicon surface, where the concentration of implanted boron atoms is well above 1e18/cm^3, as illustrated in figure 2. At a depth of 0.5 μm the boron concentration falls as low as 1e16/cm^3 and the dominating damage in this deep region consists of interstitial clusters, as calculated in figure 3. Because silicon interstitials are fast moving atoms in silicon, they can migrate quickly into regions deeper than the boron implanted region during high-temperature annealing [20], resulting in deeply located clusters with concentrations varying over a few orders of magnitude for differently annealed samples.

3.3. Hall measurement of annealed samples

From the summarized results measured by Hall and four point probing technique in table 1, we can notice that the as-implanted sample shows sheet free carrier density with one order of magnitude lower than the implantation dose and an extremely large sheet resistance. This is because implanted boron atoms are coupled with silicon interstitial clusters, which are immobile and electrically inactive, and therefore have no contributions to the majority carriers [21]. As annealing temperature and time increase, these inactivated boron-interstitial clusters started to dissolve with more stable ones requiring longer time or higher temperature to be annealed out. When boron atoms are incorporated into the substitutional lattice sites through thermal release of these clusters, they can contribute to the sheet carrier density but simultaneously forming a fair amount of ionized dopant scattering centers for carriers. Based on the analysis, it can be easily understood that the sheet carrier density in column 1 is proportional to the thermal budget, just opposite to mobility data, which shows a decreasing trend. The maximum active boron density accounts for 98.73% of the chemical boron density, indicating that prolonging annealing time at 1000 °C can no longer significantly affect the density of holes. The definition of sheet resistance is expressed as

$$R_\square = \frac{1}{x_j \sigma} = \frac{1}{q \int_0^{x_j} N_e(x) \mu \, \mathrm{d}x}, \tag{2}$$

where $N_e(x)$ is effective ionized dopant density, μ is mean mobility of majority carriers. Because of the more rapid increase of $N_e(x)$ for thermal budget increasing from the lowest to the highest, the emitter sheet resistance decreases greatly from 226 Ω/□ to 128 Ω/□.
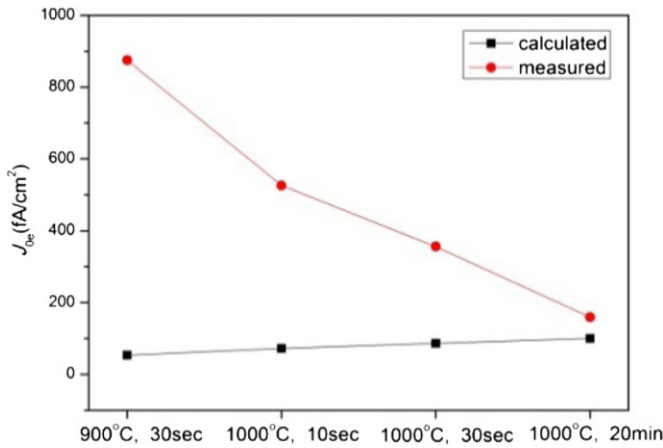
Figure 6. Measured and theoretically calculated emitter saturation current density (J_{0e}) of boron implanted samples annealed at different conditions.

3.4. Measurement of emitter saturation current density by QSSPC method

The determination of emitter saturation current density (J_{0e}) by quasi-steady state photoconductance decay (QSSPC) technique under high injection conditions is a direct method to evaluate the emitter quality for performance predictions of potential solar cells [22]. Figure 6 gives the comparison of the measured emitter saturation current density for each annealed emitter with calculated intrinsic values, based on the doping profiles at different annealing conditions illustrated in figure 2 and surface recombination velocity (S_{eff}) [23]. All the samples are double sides implanted, subsequently passivated by stacking layers of Al_2O_3/SiN_x. It is obvious that the measured J_{0e} values follow a significantly different trend from the calculated ones, which show a slight increase with increasing annealing temperature and time due to an increased integration of Auger recombination in the emitter. The highest thermal budget (FA@1000 °C, 20 min) produces the lowest measured J_{0e}, which is very close to the calculated theoretical limit of 100 fA cm^{-2}, indicating that there is no significant SRH recombination in the emitter bulk. As thermal budget decreases, however, the values of J_{0e} show drastic increase. This is in fairly good agreement with the previous result [24]. The largest deviation from the theoretical limit happens at annealing temperature of 900 °C for 30 s. This effect can be appropriately accounted for using the remnant damage theory proposed in the analysis of figure 3. Because of some more stable extended defects, the sample annealed in the furnace for a long time still shows slightly higher J_{0e} than the calculated value.

4. Performance analysis of PESC solar cells

4.1. Parameter analysis of dark I–V curves

The measured dark current–voltage (*I–V*) characteristics of the B-implanted solar cells annealed at different conditions are shown in figure 7. The reverse saturation current density drops obviously with increasing thermal budget. The injection
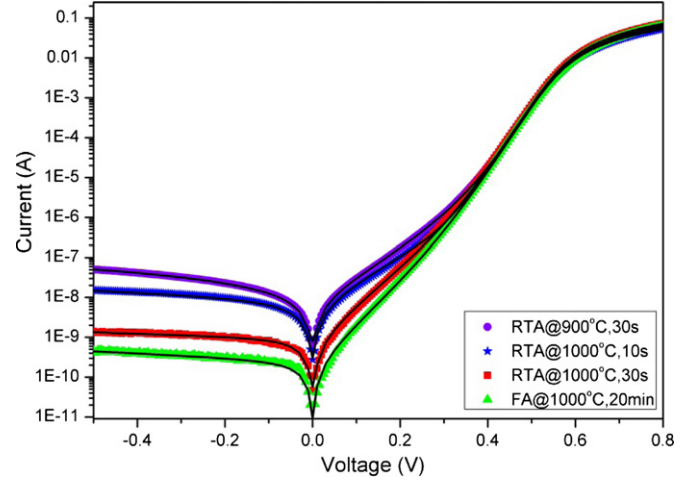

Figure 7. Plots of dark current–voltage curves of the fabricated cells annealed by RTA or FA (symbols) and their corresponding fitted curves by applying double-exponential diode model (lines).

Table 2. Diode parameter values of B-implanted solar cells obtained by fitting the dark *I–V* curves.

Ion dose (ions cm^{-2})	I_{01} (pA)	I_{0n} (nA)	n	R_s (mΩ)	R_{sh} (10^9 Ω)
900 °C, 30 s	2.39	6	2.78	3.27	1
1000 °C, 10 s	2.3	3.73	2.10	3.57	5.8
1000 °C, 30 s	2	0.8	1.88	2.51	94.2
1000 °C, 20 min	1.98	0.2	1.65	2.83	200

current density in forward bias can be explained in terms of two exponential current components. One is an ideal exponential component with ideality factor equal to 1, which corresponds to the solar operation range of 0.4–0.6 V, while the other nonideal exponential component with ideality factor in the range 2–4 dominates the lower voltage range. Extremely good fit to the experimental data near room temperature is obtained by fitting with the classical double-diode model expressed in the following form:

$$I = I_{01}[\exp(q(V - IR_s)/kT) - 1] + I_{0n}[\exp(q(V - IR_s)/nkT) - 1] + (V - IR_s)/R_{sh}, \quad (3)$$

where I_{01} and I_{0n} are the saturation current densities of the ideal and nonideal components, *n* is the ideality factor of the nonideal current components, R_s and R_{sh} are the series and shunt resistances of the device. The parameter values required to fit the experimental data are listed in table 2 for comparison.

It is commonly believed that I_{01} is closely related to recombination in the quasi-neutral region of both emitter and base, while I_{0n} reflects the overall recombination in the SCR, where possible non-annihilated defects exist as effective recombinative centers for carriers in forward bias. Table 2 shows that as annealing time and temperature increase, there is a slight decrease of I_{01}, which is perhaps due to the degradation of bulk minority carrier lifetime induced by high-temperature annealing [25]. In contrast, I_{0n} decreased by one order of magnitude, which follows the same trend as the ideality factor *n* of nonideal component. The large nonideal characteristics of junction under insufficient annealing are most likely due to,
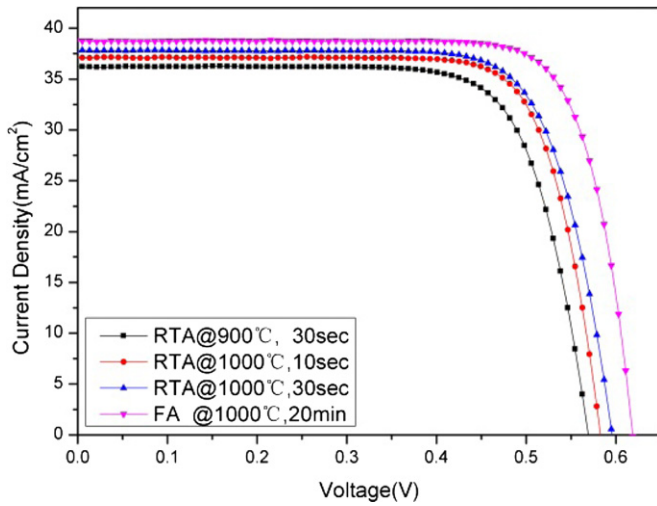
Figure 8. Measured illuminated *I–V* characteristics of the boron implanted solar cells under standard terrestrial test conditions.

Figure 9. IQE spectrum for the boron implanted solar cells as a function of annealing temperature and time.

according to the analysis aforementioned, the EOR dislocation loops in the SCR, which are resistant to resolution even in high temperature. Furthermore, the notable change of I_{0n} and n has direct impact on the photovoltaic performance of future solar cells [26]. According to the Shockley equation,

$$V_{oc} = \frac{nkT}{q} \ln\left(\frac{I_L}{I_0} + 1\right), \qquad (4)$$

where $I_0 = I_{01} + I_{0n}$, we can draw a basic conclusion that the decrease of I_{01} and I_{0n} will significantly improve the open circuit voltage by several tens of mV. The following ideal filling factor expression,

$$FF = \frac{v_{oc} - \ln(v_{oc} + 0.72)}{v_{oc} + 1}, \qquad (5)$$

where $v_{oc} = \frac{v_{oc}}{nkT/q}$, n is the weighted cell ideality factor, indicates that the bigger n is, the lower FF will be. In summary, these results demonstrate that a higher thermal budget is required for a more sufficient damage removal in SCR in boron implanted emitter, as observed by previous researches [27, 28].

4.2. Analysis of illuminated I–V characteristics

The measured illuminated *I–V* curves of solar cells annealed with different thermal budgets show obvious distinctions as demonstrated in figure 8. Considering that all the cells are fabricated with identical processing conditions and structural configuration in clean room as the same batch, these distinctions can only be attributed to difference of emitter quality. To accurately compare the dependence of cell performance on annealing conditions, the extracted parameters, including open circuit voltage (V_{oc}), short circuit current density (J_{sc}), filling factor (FF) and efficiency, are listed in table 3. The implied open circuit voltage in the last column, measured by QSSPC technique, is uniformly 20 mV higher than the practical V_{oc} of correspondingly finished devices, which demonstrates the high level of subsequent processing stability after junction formation. It is obvious that all the performance parameters show an increasing trend as thermal budget increases, reaching remarkable agreement
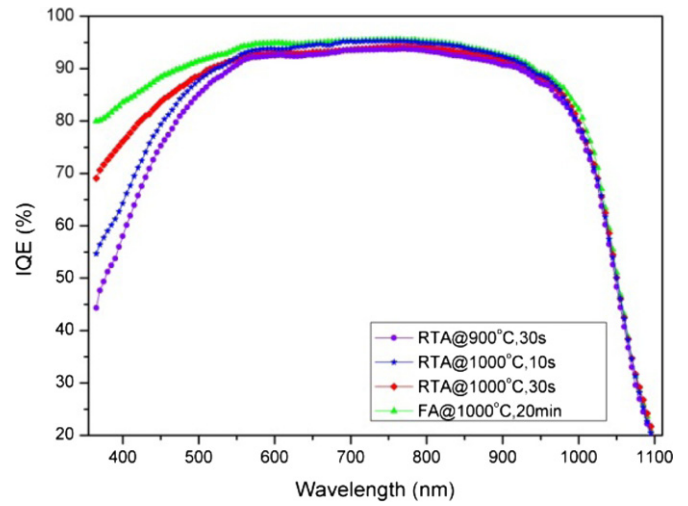
with the previous results by [10] indicating that the quality of boron implanted emitters has been improved. Specifically, the obvious increase of V_{oc} and J_{sc} confirms the reduced recombination inside the emitter, in accordance with the results of measured J_{0e} and fitted I_{0n}. In addition, the FF follows the same trend with ideality factor n, as is discussed in equation (5). In the present analysis, the influence of series resistance on FF is excluded in that the metallization schema is identical for all the fabricated solar cells. A maximum cell efficiency (measured by aperture area) of 18.85% is obtained at FA conditions for 20 min but with relatively low V_{oc}, indicating possible remnant defects are still present in emitter. It is thus indispensable to carry out further optimization of annealing conditions in tube furnace to realize sufficient damage removal.

4.3. Analysis of internal quantum efficiency

The influence of annealing conditions on internal quantum efficiency (IQE) of the fabricated solar cells is compared in figure 9. The IQE, defined as the number of carrier pairs generated per photon absorbed, characterizes the recombination active region inside the devices. The four curves, we can find, differ noticeably in the short wavelength band ranging from 330 to 600 nm, while at wavelength longer than 600 nm the cells annealed at higher thermal budget gain slightly higher responses. Because of higher short wavelength responses, the furnace annealed solar cells produce the highest V_{oc} and J_{sc} in illuminated *I–V* measurement, suggesting that the damage in emitter has been restored with higher degree than those solar cells annealed by RTA. This trend, highly consistent with the measurement results of RBS and J_{0e}, provides some guidance for us when selecting annealing conditions for boron implanted emitters: the temperature should be at least 1000 °C with duration of at least several minutes to ensure a sufficient annealing out damage. Furthermore, the subtle differences of responses in wavelength range longer than 600 nm are due to the degradation of bulk lifetime caused by high-temperature processing and thus account for the I_{01} differences discussed

Table 3. Cell performance parameters under illumination after annealing at different conditions.

Annealing condition	V_{oc}(mV)	J_{sc}(mA cm^{-2})	FF (%)	Efficiency (%)	Implied V_{oc}(mV)
900 °C, 30 s	569.4	36.2	74.6	15.38	588
1000 °C, 10 s	582.4	37.1	77	16.64	603
1000 °C, 30 s	595.8	37.8	77.6	17.48	615
1000 °C, 20 min	619	38.7	78.7	18.85	641

in section of 4.1. The near infrared response above 1000 nm shows only a slight difference in terms of different annealing conditions, revealing that the annealing steps show no obvious impact on the performance of phosphorus back surface field. This is in sharp contrast to boron implanted emitter. It should be noted that the selected annealing temperatures in this study are all above 950 °C, which is sufficient for phosphorus activation and damage removal as the published results demonstrate in [29, 30]. The four-point probe measurement shows that all the phosphorus implanted back surface regions after different annealing steps produce sheet resistance below $30\Omega/\square$, giving further evidence for the fully activated, damage-free region of BSF.

5. Conclusions

The effects of annealing on the properties of B-implanted Si for n-type PESC solar cells were investigated by comparing RTA and FA conditions. By way of TCAD process simulation tools, the profiles of dopants and remnant clusters after annealing at different conditions were displayed. It was found from the simulation that the mechanism of TED is especially striking in the first few seconds during high-temperature annealing. Apart from this theoretical calculation of residual damage in emitter, QSSPC, Hall and RBS techniques are simultaneously employed to probe into the effects of annealing on the electrical properties of B-implanted samples. Compared with annealed samples with lower thermal budgets, the one that received annealing at 1000 °C for 20 min exhibited the lowest J_{0e} and damage spectra and the highest free carrier density. All the measured results indicated that boron implanted samples annealed at 1000 °C or lower for tens of seconds were far less enough to activate dopants and recover the damage induced by implantation. Finally, PESC solar cells were fabricated and measured to check the emitter property at device level. The champion cell, which was annealed in furnace for 20 min., had maximum V_{oc} of 619 mV, J_{sc} of 38.7 mA cm^{-2}, FF of 78.7% and efficiency of 18.85%, whereas those receiving lower thermal budgets exhibited lower performance. The limiting factors of performance were diagnosed by fitting dark I–V curves using double-diode equation and IQE measurement. It was found that emitters with RTA showed increased recombination, revealed by the low short wavelength responses, high saturation current density (I_{0n}) and high ideality factor n of nonideal component of current.

References

[1] Rohatgi A, Meier D L, McPherson B, Ok Y-W, Upadhyaya A D, Lai J-H and Zimbardi F 2012 *Energy Procedia* **15** 10
[2] www.vsea.com/products.nsf/docs/solion
[3] Bateman N, Sullivan P, Reichel C, Benick J and Hermle M 2011 *Energy Procedia* **8** 509
[4] Benick J and Bateman N 2010 *Proc. 25th European Photovoltaic Solar Energy Conf. and Exhibition (Valencia, Spain)* p 1169
[5] Lowndes D H, Cleland J W, Christie W H, Eby R E, Jellison G E, Narayan J, Westbrook R D, Wood R F, Nilson J A and Dass S C 1982 *Appl. Phys. Lett.* **41** 938
[6] Usami A, Yoshida N and Inoue Y 1983 *IEEE Electron Device Lett.* **4** 166
[7] Narayan J and Young R T 1983 *Appl. Phys. Lett.* **42** 466
[8] Hermann A M and Weinberg I 1979 *Bull. Am. Phys. Soc.* **24** 273
[9] Koji T, Tseng W F, Mayer J W and Suganuma T 1979 *Solid-State Electron.* **22** 335
[10] Noel S, Lautenschlager H and Muller J C 2000 *Semicond. Sci. Technol.* **15** 322
[11] Florakis A, Janssens T, Rosseel E, Douhard B, Delmotte J, Cornagliotti E, Poortmans J and Vandervorst W 2012 *Energy Procedia* **27** 240
[12] Stolk P A, Gossmann H J, Eaglesham D J, Jacobson D C, Rafferty C S, Gilmer G H, Jaraiz M, Poate J M, Luftman H S and Haynes T E 1997 *J. Appl. Phys.* **81** 6031
[13] Law M E 1988 Two dimensional numerical simulation of dopant diffusion in silicon *PhD Thesis* Department of Electrical Engineering, Stanford University
[14] Sadigh B, Lenosky T J, Theiss S K, Caturla M-J, Diaz de la Rubia T and Foad M A 1999 *Phys. Rev. Lett.* **83** 4341
[15] Ryssel H and Ruge I 1983 *Ion Implantation* (Berlin: Springer)
[16] De Salvador D, Napolitani E, Bisognin G, Carnera A, Bruno E, Mirabella S, Impellizzeri G and Priolo F 2005 *Appl. Phys. Lett.* **87** 221902
[17] Claverie A, Colombeau B, De Mauduit B, Bonafos C, Hebras X, Ben Assayag G and Cristiano F 2003 *Appl. Phys. A* **76** 1025
[18] Claverie A, Colombeau B, Ben Assayag G, Bonafos C, Cristiano F, Omri M and de Mauduit B 2000 *Mater. Sci. Semicond. Process.* **3** 269
[19] Feldman L C 1982 *Materials Analysis by Ion Channeling* (New York: Academic)

[20] Macdonald D H, Maeckel H, Doshi S, Brendle W, Cuevas A, Williams J S and Conway M J 2003 *Appl. Phys. Lett.* **82** 2987

[21] Angelucci R, Cembali F, Negrini P, Servidori M and Solmi S 1987 *J. Electrochem. Soc.* **134** 3130

[22] Sinton R A and Cuevas A 1996 *Appl. Phys. Lett.* **69** 2510

[23] McIntosh K R and Altermatt P P 2010 *Proc. 35th IEEE Photovoltaic Specialists Conf. (Honolulu, HI)* p 2188

[24] Mok K R C, Naber R C G and Nanver L K 2012 *Proc. 19th Int. Conf. on Ion Implantation Technology (Valladolid, Spain)* p 245

[25] Macdonald D and Geerligs L J 2004 *Appl. Phys. Lett.* **85** 4061

[26] Goetzberger A, Knobloch J and Voss B 1998 *Crystalline Silicon Solar Cells* (New York: Wiley)

[27] Müller R, Benick J, Bateman N, Schön J, Reichel C, Richter A, Hermle M and Glunz S W 2014 *Sol. Energy Mater. Sol. Cells* **120** 431

[28] Peterstr S and Holmen G 1974 *Phys. Scr.* **10** 142

[29] Kang M G, Lee J-H, Boo H, Tark S J, Hwang H C, Hwang W J, Kang H O and Kim D 2012 *Curr. Appl. Phys.* **12** 1615

[30] Lanterne A, Gall S, Manuel S, Monna R, Ramappa D, Yuan M, Rivalin P and Tauzin A 2012 *Energy Procedia* **27** 580